Nanosized Cation-Deficient Fe–Ti Spinel: A Novel Magnetic Sorbent for Elemental Mercury Capture from Flue Gas

Shijian Yang,[†] Yongfu Guo,[†] Naiqiang Yan,*,[†] Daqing Wu,[‡] Hongping He,[‡] Zan Qu,[†] Chen Yang,[†] Qin Zhou,[§] and Jinping Jia[†]

[†]School of Environmental Science and Engineering, Shanghai Jiao Tong University, 800 Dong Chuan Road, Shanghai, 200240 P. R. China

[‡]Guangzhou Institute of Geochemistry, Chinese Academy of Sciences, 511 Kehua Street, Wushan, Tianhe District, Guangzhou, 510640 P. R. China

[§]State Key Laboratory of Environmental Aquatic Chemistry, Research Center for Eco-Environmental Sciences, Chinese Academy of Sciences, 18 Shuangqing Road, Haidian District, Beijing, 100085 P. R.China

ABSTRACT: Nonstoichiometric Fe–Ti spinel $(Fe_{3-x}Ti_x)_{1-\delta}O_4$ has a large amount of cation vacancies on the surface, which may provide active sites for pollutant adsorption. Meanwhile, its magnetic property makes it separable from the complex multiphase system for recycling, and for safe disposal of the adsorbed toxin. Therefore, $(Fe_{3-x}Ti_x)_{1-\delta}O_4$ may be a promising sorbent in environmental applications. Herein, $(Fe_{3-x}Ti_x)_{1-\delta}O_4$ is used as a magnetically separable sorbent for elemental mercury capture from the flue gas of coal-fired power plants. $(Fe_2Ti)_{0.8}O_4$ shows a moderate capacity (about 1.0 mg g^{-1} at 250 °C) for elemental mercury capture in the presence of 1000 ppmv of SO_2. Meanwhile, the sorbent can be readily separated from the fly ash using magnetic separation, leaving the fly ash essentially free of sorbent and adsorbed mercury.

KEYWORDS: Fe–Ti spinel, cation vacancy, elemental mercury, capture capacity, magnetic sorbent
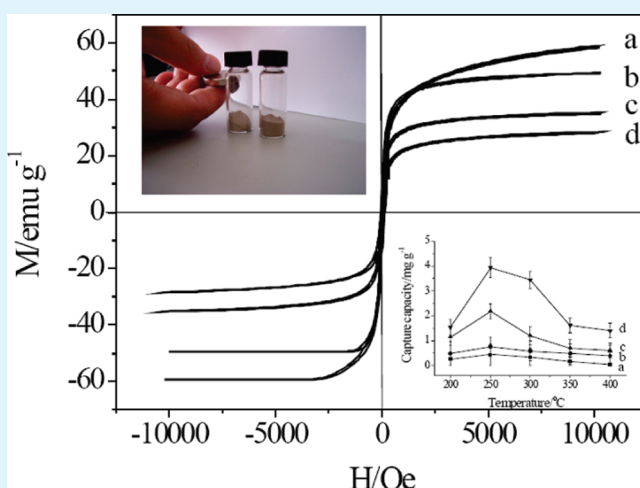
1. INTRODUCTION

Synthesis of magnetic nanoparticles has long been of scientific and technological interest[1] due to their potential applications in tissue imaging,[2] drug delivery,[3] information storage,[4] and magnetically separable catalyst/sorbents.[5,6] Spinel ferrites are of great fundamental and technological importance due to their structural, electronic, magnetic, and catalytic properties.[7] An interesting feature of spinel ferrites is the possibility to replace iron cations by other metal cations while maintaining the spinel structure.[8] The physicochemical properties of spinel ferrites are strongly dependent on the site, nature, and amount of metal incorporated into the structure.

Two Fe^{3+} cations in magnetite (Fe_3O_4) can be substituted by one Ti^{4+} cation and one Fe^{2+} cation to form titanomagnetite $(Fe_{3-x}Ti_xO_4)$. The presence of Ti^{4+} in the spinel structure can improve its thermal stability.[5] It is interesting that $Fe_{3-x}Ti_xO_4$ can be oxidized to nonstoichiometric Fe–Ti spinel $(Fe_{3-x}Ti_x)_{1-\delta}O_4$ while maintaining the spinel structure.[8] The oxidation of $Fe_{3-x}Ti_xO_4$ can be described as

$$(1-\delta)Fe_{3-x}Ti_xO_4 + 2\delta O_2 \longrightarrow (Fe_{3-x}Ti_x)_{1-\delta}\square_{3\delta}O_4 \quad (1)$$
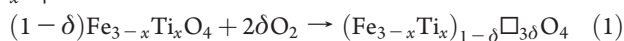
where $\square$ is the cation vacancy. δ is equal to $(1+x)/(9+x)$ if all Fe^{2+} cations in $Fe_{3-x}Ti_xO_4$ are oxidized to Fe^{3+} cations.[9] The oxidization of $Fe_{3-x}Ti_xO_4$ to $(Fe_{3-x}Ti_x)_{1-\delta}O_4$ is similar to the oxidization of Fe_3O_4 to γ-Fe_2O_3. The oxidization of Fe_3O_4 to γ-Fe_2O_3 involves a reduction in the number of Fe atoms per unit cell from 24 in Fe_3O_4 to 64/3 in γ-Fe_2O_3. The oxidization of Fe_3O_4 proceeds by outward migration of Fe^{2+} cations toward the surface of the crystal together with the creation of cation vacancies. On the surface, Fe^{2+} cations are oxidized and interact with adsorbed oxygen to form a rim of γ-Fe_2O_3. In γ-Fe_2O_3, eight cations occupy tetrahedral sites and the remaining cations are randomly distributed over the octahedral site. The vacancies in γ-Fe_2O_3 are confined to the octahedral sites. The detailed distribution of cations and vacancies in $(Fe_{3-x}Ti_x)_{1-\delta}O_4$ is not fully understood.[8]

Cation vacancies on $(Fe_{3-x}Ti_x)_{1-\delta}O_4$ can provide the active sites for pollutant adsorption. Furthermore, the magnetic property

makes it possible to separate $(Fe_{3-x}Ti_x)_{1-\delta}O_4$ from the complex multiphase system for recycling, and for safe disposal of the adsorbed toxin. Therefore, $(Fe_{3-x}Ti_x)_{1-\delta}O_4$ may be an environmental-friendly sorbent for pollutant control.

Mercury is a major pollutant because of its toxicity, mobility, and bioaccumulation in the ecosystem and food chain. The emission of mercury from anthropogenic activities is a serious concern in both developed and developing countries.[10] Coal-fired utilities are the main source of mercury emission from anthropogenic activities. In addition to particulate-bound mercury (Hg^P), both elemental mercury (Hg^0) and oxidized mercury (Hg^{2+}) are present as the gaseous mercury in the flue gas of coal-fired utilities.[10,11] Particulate-bound mercury and oxidized mercury (mainly $HgCl_2$) can be effectively removed by particulate control devices and wet scrubbing or SO_2 control devices, respectively.[11] Because elemental mercury is not soluble in water, it is difficult to remove with currently available removal devices.[12] Therefore, elemental mercury can be a major species in the exhaust gas of coal-fired utilities.[13] In China, the total mercury concentrations in the flue gas from coal-fired boilers are in the range of $1.92-27.2\ \mu g\ m^{-3}$, and elemental mercury accounts for $66-94\%$ of the total mercury.[14]

Many technologies have been investigated to control the emission of elemental mercury from flue gas, including sorbents, catalysts employed upstream of wet scrubbers, and photochemical oxidations.[10,12,15−30] Now, the mercury-sorbent material is extremely restricted in the application for at least three reasons: material recovery, removal of toxin from the industrial waste,[31] and cost of operation. First, the spent sorbent for this particular application is often collected as a mixture with greater than 99% of ultrafine fly ash particles by particulate control devices. It will be extremely difficult and impractical to reclaim the sorbent from the fly ash mixture for regeneration. Second, if the spent sorbent is not effectively removed from the fly ash mixture, the fly ash will be contaminated with the mercury-loaded sorbent. If the mercury-contaminated fly ash is used as a cement additive, mercury may be released in the cement plant during the calcination process. Third, the material must be cheap and operation must be easy.

To separate the sorbent from the majority of the fly ash stream, the injection of activated carbon upstream of a small secondary baghouse filtration system on the back-end of the power plant was investigated in the United States.[32,33] The separation of sorbent from the fly ash may be more easily achieved by the magnetic property of the sorbent. A magnetic sorbent MagZ-Ag^0 was once used to capture elemental mercury from flue gas,[31,34] but the sorbent was expensive.

Herein, a series of nanosized nonstoichiometric Fe−Ti spinel were used as magnetic sorbents for gaseous elemental mercury capture. Nonstoichiometric Fe−Ti spinel was synthesized using a coprecipitation method and characterized using X-ray diffraction (XRD), H_2 temperature-programmed reduction (TPR), N_2 adsorption/desorption isotherm, transmission electron microscopy (TEM), and magnetization measurement. Then, a packed-bed reactor system was used to preliminarily investigate the performance of nanosized nonstoichiometric Fe−Ti spinel for elemental mercury capture.

2. MATERIALS AND METHODS

2.1. Sample Preparation. Nanosized $Fe_{3-x}Ti_xO_4$, the precursor of $(Fe_{3-x}Ti_x)_{1-\delta}O_4$, was prepared using a coprecipitation method at room temperature.[35−38] Suitable amounts of ferrous

sulfate, ferric trichloride, and titanium tetrachloride were dissolved in a HCl solution. pH (<1) was low enough to prevent any titanium or iron oxide and hydroxide precipitation. This mixture was added to an ammonia solution leading to an instantaneous precipitation of titanium ferrites according to the following equation:

$$(2-2x)Fe^{3+} + (1+x)Fe^{2+} + xTi^{4+} + 8OH^- \rightarrow Fe_{3-x}Ti_xO_4 + 4H_2O$$

$$(2)$$
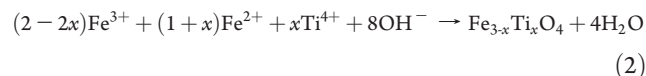
During the reaction, the system was continuously stirred at 800 rpm. The particles were then separated by centrifugation at 4500 rpm for 5 min and washed with distilled water followed by a new centrifugation. After 4 washings, the particles were collected and dried in a vacuum oven at 105 °C for 24 h. The characterization of XRD and Mössbauer in previous studies demonstrated that synthesized $Fe_{3-x}Ti_xO_4$ was spinel structure, and Ti was incorporated into its structure.[5,6,35−38]

Maghemite (γ-Fe_2O_3 or $Fe_{2.67}O_4$) was obtained after the thermal treatment of Fe_3O_4 at 250 °C under air for 3 h. $(Fe_{3-x}Ti_x)_{1-\delta}O_4$ ($x \neq 0$) was obtained after the thermal treatment of $Fe_{3-x}Ti_xO_4$ at 350 °C under air for 3 h. Under such conditions, all Fe^{2+} cations were expected to be oxidized to Fe^{3+} cations.

2.2. Sample Characterization. The crystal structure was determined using an X-ray diffractometer (Rigaku, D/max-2200/PC) between 10° and 80° at a step of 7° min^{-1} operating at 30 kV and 30 mA using Cu Kα radiation. The Brunauer−Emmett−Teller (BET) surface area was determined using a nitrogen adsorption apparatus (Micromeritics, ASAP 2010 M+C). The sample was outgassed at 200 °C before BET measurement. The TPR profile was recorded on a chemisorption analyzer (Micromeritics, ChemiSorb 2720 TPx) under a 10% hydrogen/90% nitrogen gas flow (20 cm^3 min^{-1}) at a rate of 10 °C min^{-1}. The saturated magnetization was determined using a vibrating sample magnetometer (VSM, model JDM-13) at room temperature. The TEM image was performed on a JEOL JEM-2010 TEM. The micrographs were obtained in the bright-field imaging mode at an acceleration voltage of 200 kV. XPS (Thermo ESCALAB 250) was used to determine the binding energies of Fe 2p, Ti 2p, S 2p, O 1s, and Hg 4f with Al Kα (hv = 1486.6 eV) as the excitation source. The C 1s line at 284.6 eV was taken as a reference for the binding energy calibration.

2.3. Elemental Mercury Capture. The assembly used for elemental mercury capture is similar to that previously described by Granite et al. (shown in Figure 1).[18] It consisted of an elemental mercury permeation tube, a packed-bed reactor, a cold vapor atomic absorption spectrometer (CVAAS), and an online data acquisition system. A flow of air passed through the permeation tube and then yielded a gas with a stable concentration of elemental mercury. A temperature control device was employed to keep the reactor at desired temperatures. Before each test, the gas containing elemental mercury first passed through the empty tube, and then entered the CVAAS to determine the baseline. When the concentration of elemental mercury had fluctuated within ±5% for more than 30 min, the gas was diverted to the adsorbent bed for the test. An exact amount of sorbent was inserted in the middle of the column reactor and then packed with quartz wool to support the sorbent layer and avoid its loss. It was demonstrated that quartz wool has no ability for elemental mercury capture.[39]

To preliminarily estimate the performance for elemental mercury capture, $(Fe_{3-x}Ti_x)_{1-\delta}O_4$ was first tested under air.

210

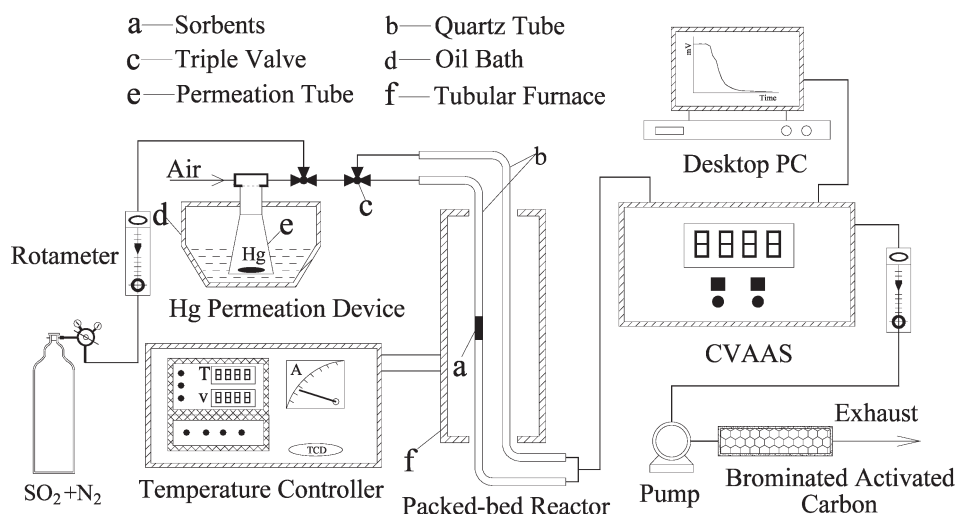dx.doi.org/10.1021/am100835c |ACS Appl. Mater. Interfaces 2011, 3, 209–217

Figure 1. Experimental system for packed-bed test.

The inlet gas contained about 1.10 mg Nm^{-3} ($\pm 20\%$) of elemental mercury and 2% of H$_2$O with a feed of 12 L h^{-1}. The test time for (Fe$_{3-x}$Ti$_x$)$_{1-\delta}$O$_4$ ($x \neq 0$) was about 10 h, but that for γ-Fe$_2$O$_3$ was about 4 h. For each test, the sorbent mass was 30 mg, the gas space velocity was about 1.2×10^6 h^{-1}, and the reaction temperatures varied from 200 to 400 °C.

The chemical composition in the flue gas significantly affects elemental mercury adsorption by sorbents.[40] The components in the real coal combustion flue gas that can influence elemental mercury capture are mainly the high concentration of SO$_2$.[41,42] SO$_2$ molecules may compete with gaseous elemental mercury for the active sites. The concentration of SO$_2$ in real flue gas is about 10^4–10^5 times that of elemental mercury (v/v).[41,43] Therefore, the effect of a high concentration of SO$_2$ on elemental mercury capture was investigated. The gas contained about 0.48 mg Nm^{-3} of elemental mercury, 2% of H$_2$O, 2.8 g Nm^{-3} (1000 ppmv) of sulfur dioxide, and 10% of O$_2$ with a feed of 12 L h^{-1}. For each test, the sorbent mass was 50 mg and the gas space velocity was about 7.2×10^5 h^{-1}.

The concentration of elemental mercury in the gas was analyzed online using a SG-921 CVAAS (Jiangsu Jiangfen). Furthermore, the concentration of Hg^{2+} at the reactor exit was determined using the Ontario Hydro Method (OHM).[14] The breakthrough curve was generated by plotting the CVAAS voltage signal.

3. RESULTS AND DISCUSSION

3.1. Characterization. XRD patterns of synthesized (Fe$_{3-x}$Ti$_x$)$_{1-\delta}$O$_4$ are shown in Figure 2. Their characteristic peaks correspond very well to the standard card of maghemite (JCPDS 39-1346). If there were some amorphous TiO$_2$ in synthesized Fe$_{3-x}$Ti$_x$O$_4$, it should transform to rutile (or anatase) after the calcination at 350 °C for 3 h.[5] As shown in Figure 2, the characteristic peaks corresponding to rutile and anatase did not appear. This suggests that there was no amorphous TiO$_2$ in synthesized Fe$_{3-x}$Ti$_x$O$_4$,[5] so Ti was introduced into the spinel structure of synthesized (Fe$_{3-x}$Ti$_x$)$_{1-\delta}$O$_4$. The incorporation of Ti into the spinel structure was also demonstrated by the characterization of electron energy loss spectroscopy (EELS), X-ray adsorption near edge structure (XANES), and extended X-ray adsorption fine structure (EXAFS) in previous research.[36,38]
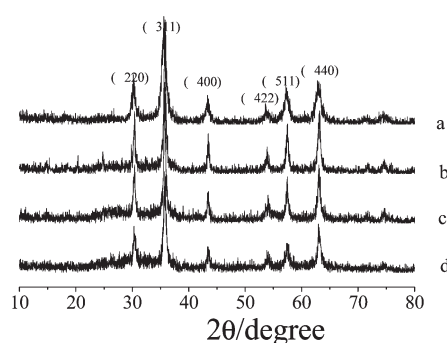

Figure 2. XRD patterns of synthesized (Fe$_{3-x}$Ti$_x$)$_{1-\delta}$O$_4$: (a) $x = 0$; (b) $x = 0.3$; (c) $x = 0.7$; (d) $x = 1$.

Table 1. δ, Crystal Size, BET Surface Area, and Amount of Cation Vacancies on the Surface

x	δ	crystal size (nm)	BET surface area (m^2 g^{-1})	the amount of cation vacancies on the surface (m^2 g^{-1})
0	0.11 ± 0.02	14 ± 2	101 ± 10	4.7 ± 0.5
0.3	0.14 ± 0.02	26 ± 4	28.2 ± 3	1.7 ± 0.2
0.7	0.18 ± 0.02	24 ± 4	51.3 ± 5	3.9 ± 0.4
1	0.20 ± 0.02	14 ± 2	125 ± 12	11 ± 1.1

The calculated lattice parameters of synthesized samples were all about 0.834 nm, consistent with previous research.[35] Crystal sizes of synthesized samples were calculated with the Scherrer's equation.[5] The nucleation of Ti^{4+} preferred to yield an amorphous hydroxide or hydroxide oxide,[44] so the crystal size of synthesized (Fe$_{3-x}$Ti$_x$)$_{1-\delta}$O$_4$ ($x \neq 0$) decreased with the increase of Ti content (shown in Table 1). This result was consistent with the observation of BET surface area (shown in Table 1).

TEM images (Figure 3) revealed irregular agglomerated nanoparticles of iron oxide (darker contrast in the figures). As shown in Figure 3a, synthesized γ-Fe$_2$O$_3$ was near spherical, and the particle sizes were about 10–20 nm. Many particles with bigger size appeared in (Fe$_{3-x}$Ti$_x$)$_{1-\delta}$O$_4$ ($x \neq 0$) (shown in Figure 3b–d). This may result from the higher calcination
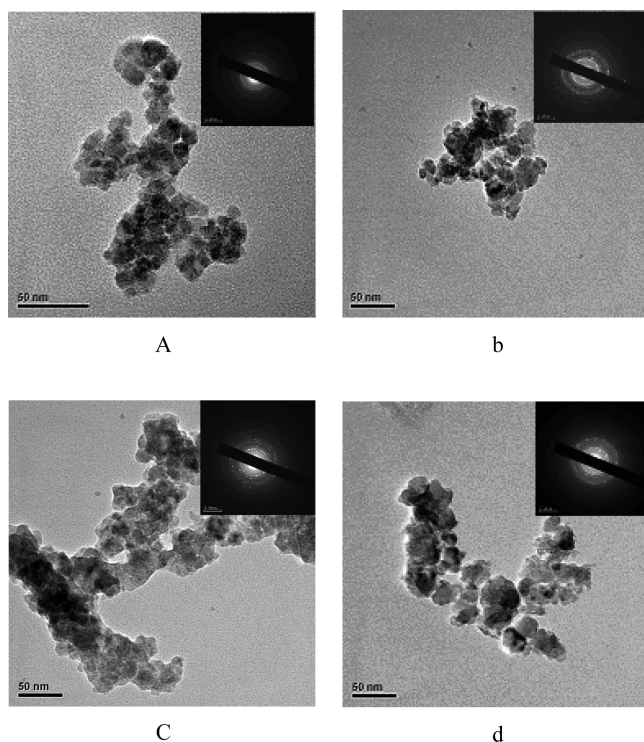
Figure 3. TEM images of synthesized $(Fe_{3-x}Ti_x)_{1-\delta}O_4$: (a) $x = 0$; (b) $x = 0.3$; (c) $x = 0.7$; (d) $x = 1$. The insets show the selected area electron diffraction patterns of the nanoparticles.
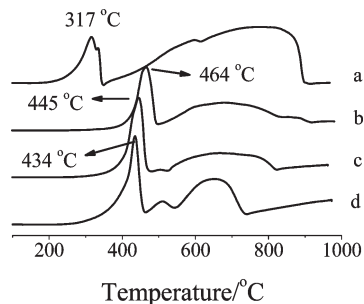

Figure 4. H_2-TPR profiles of synthesized $(Fe_{3-x}Ti_x)_{1-\delta}O_4$: (a) $x = 0$; (b) $x = 0.3$; (c) $x = 0.7$; (d) $x = 1$.

temperature. Supporting information was obtained from the selected area electron diffraction patterns (SAED). All samples showed obvious polycrystalline diffraction rings, as a consequence of the small crystallite sizes, which can be ascribed to the reflections of (200), (311), (400), (511), and (440) crystallographic planes of a cubic spinel phase. The lattice parameters determined from the electron diffraction rings were all about 0.834 nm, which were hinted by XRD results.

H_2-TPR technique can be employed to study the reducibility.[45] H_2-TPR profiles of synthesized $(Fe_{3-x}Ti_x)_{1-\delta}O_4$ are illustrated in Figure 4. TPR profile recorded from γ-Fe_2O_3 showed two obvious reduction peaks. The peak centered at about 317 °C was assigned to the reduction of γ-Fe_2O_3 to Fe_3O_4, which was demonstrated by the Mössbauer observation.[37] The broad peak at higher temperature was attributed to the reduction of Fe_3O_4 to Fe.[46,47] TPR profiles of $(Fe_{3-x}Ti_x)_{1-\delta}O_4$ ($x \neq 0$) also showed two obvious reduction peaks. The first set of peaks centered at

about 450 °C corresponded to the reduction of $(Fe_{3-x}Ti_x)_{1-\delta}O_4$ to $Fe_{3-x}Ti_xO_4$, and the set of broad peaks at higher temperature were attributed to the reduction of $Fe_{3-x}Ti_xO_4$ to Fe and TiO_2.[37,48] The presence of the peak at about 510 °C in the TPR profile of $(Fe_2Ti)_{0.8}O_4$ may indicate that a transition phase ($FeTiO_3$ or $FeTi_2O_5$) appeared during the reduction of Fe_2TiO_4 to Fe and TiO_2.[48]

In comparison with γ-Fe_2O_3, a strong displacement of the first peak to about 450 °C occurred in the TPR profiles of $(Fe_{3-x}Ti_x)_{1-\delta}O_4$ ($x \neq 0$). This may indicate that Ti was incorporated into the spinel structure.[49]

The fist step of $(Fe_{3-x}Ti_x)_{1-\delta}O_4$ reduction can be described as follows:

$$(Fe_{3-x}Ti_x)_{1-\delta}O_4 + 4\delta H_2 \rightarrow (1 - \delta)Fe_{3-x}Ti_xO_4 + 4\delta H_2O \quad (3)$$
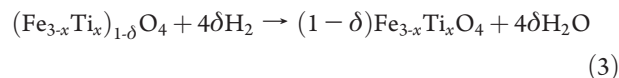
As shown in eq 3, the consumption of H_2 for the reduction of $(Fe_{3-x}Ti_x)_{1-\delta}O_4$ to $(Fe_{3-x}Ti_x)_{1-\delta}O_4$ would obviously increase with the increase of Ti content, which was demonstrated by the TPR analysis. TPR analysis shows that the area ratio of the first peak to the total TPR profile increased from 12.5% for γ-Fe_2O_3 to 31% for $(Fe_2Ti)_{0.8}O_4$. This indicates that the reducibility (i.e., oxidative capacity) of $(Fe_{3-x}Ti_x)_{1-\delta}O_4$ at lower temperatures obviously improved with the increase of Ti content in $(Fe_{3-x}Ti_x)_{1-\delta}O_4$.

Surface information of synthesized $(Fe_2Ti)_{0.8}O_4$ was analyzed by XPS. XPS spectra over the spectral regions of Fe 2p, Ti 2p, and O 1s were evaluated (shown in Figure 5a−c). The Fe peaks (shown in Figure 5a) were assigned to oxidized Fe species, more likely Fe^{3+} type species.[50] The binding energies centered at about 710.3 and 711.2 eV may be assigned to Fe^{3+} in the spinel structure, and the binding energy centered at about 712.5 eV may be ascribed to Fe^{3+} bonded with hydroxyl groups. This assignment was supported by the satellite component observed at about 719.2 eV, which is the fingerprint of Fe^{3+} species.[51] The Ti peaks (shown in Figure 5b) were assigned to Ti 2p 1/2 (464.3 eV) and Ti 2p 3/2 (458.6 eV) of Ti^{4+}. The O 1s peaks (shown in Figure 5c) mainly centered at about 530.1 eV, as expected for the transition metal oxides. Other oxygen species centered at about 531.5 eV was also observed, which was assigned to −OH.[50,51]

A key feature of the novel sorbent is its magnetic property, which makes it simple to separate the sorbent from the complex multiphase system. The saturated magnetization of synthesized $(Fe_{3-x}Ti_x)_{1-\delta}O_4$ ($x = 0$, 0.3, 0.7, and 1) were 59.0, 49.5, 35.2, and 28.5 emu g^{-1}, respectively. They all exhibited superparamagnetism with a minimized coercivity and a negligible magnetization hysteresis (shown in Figure 6). The magnetization characteristics ensure that the magnetic sorbents do not become permanently magnetized after being exposed to an external magnetic field, which in turn permit the magnetic particles to be redispersed without aggregation when the magnetic field is removed.[31]

Although the crystal sizes of synthesized samples were all less than 30 nm, their particulate sizes were much bigger than 10 μm due to the agglomeration after the thermal treatment. The magnetic sorbent can be recovered in situ by a two-step process. Particulates can first be removed from the flue gas by an electrostatic precipitator, followed by the magnetic separation of the sorbent and adsorbed mercury from the fly ash. Previous research has demonstrated that the magnetic sorbent MagZ-Ag^0 can be easily separated from fly ash.[31,34] The photograph inserted in Figure 6 shows the result of separating $(Fe_2Ti)_{0.8}O_4$ from the

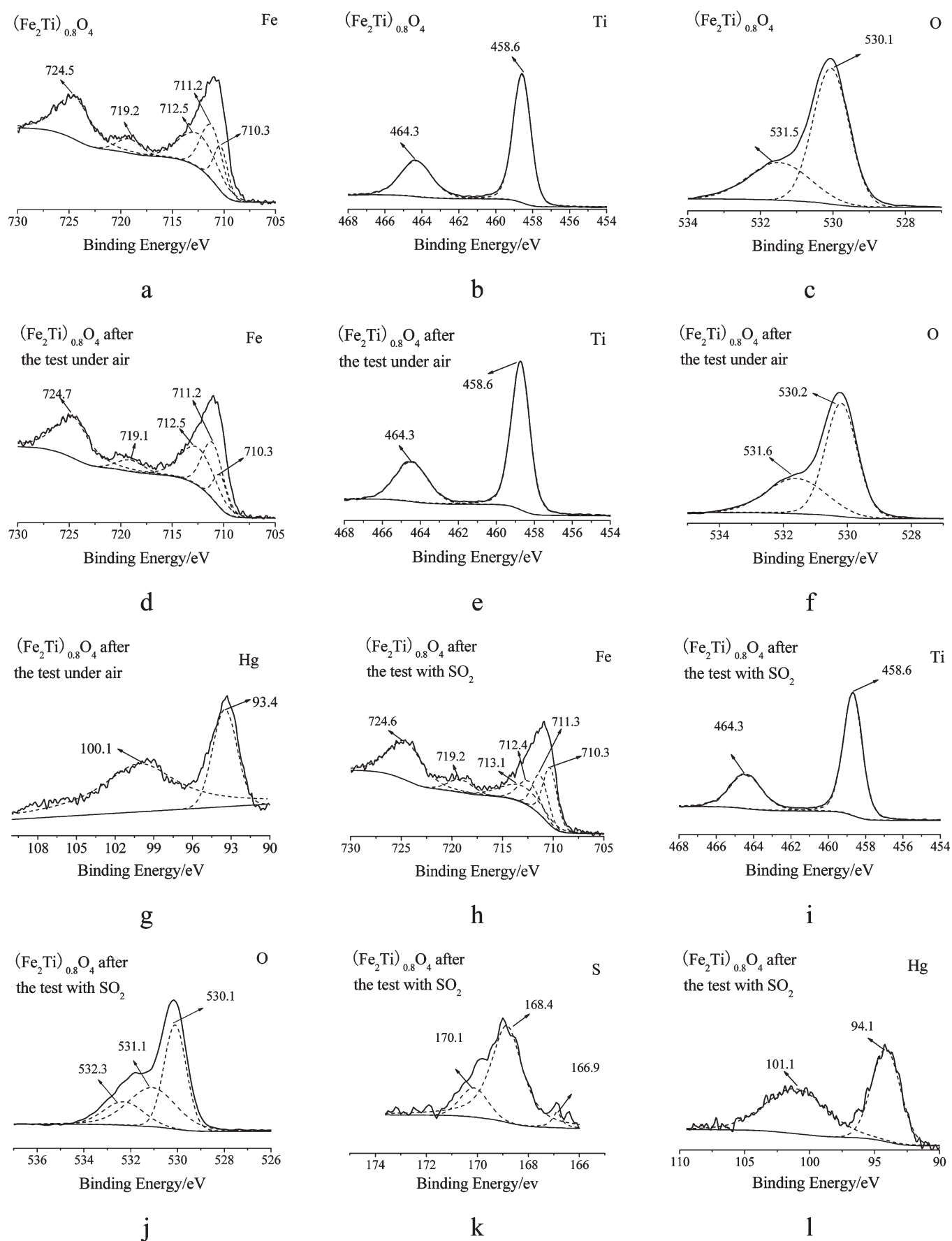**Figure 5.** XPS spectra of $(Fe_2Ti)_{0.8}O_4$ over the spectral regions of Fe 2p, Ti 2p, O 1s, Hg 4f, and S 2p.

213

dx.doi.org/10.1021/am100835c |*ACS Appl. Mater. Interfaces* 2011, 3, 209–217

mixture with 10 g of fly ash and 1 g of $(Fe_2Ti)_{0.8}O_4$ by a normal magnet. After $(Fe_2Ti)_{0.8}O_4$ was separated from the mixture, the content of Fe in the fly ash did not increase. This demonstrates that $(Fe_2Ti)_{0.8}O_4$ can be separated from the fly ash using magnetic separation, leaving the fly ash essentially free of sorbents and adsorbed mercury. However, the mass of $(Fe_2Ti)_{0.8}O_4$ increased because some fly ash adsorbed on it.

3.2. Elemental Mercury Capture under Air. The determination of Hg^{2+} concentration showed that there was little Hg^{2+} in the gas after passing through the reactor tube with the sorbent, so the reduced amount of elemental mercury was captured by the sorbent. The breakthrough curves of elemental mercury capture by $(Fe_2Ti)_{0.8}O_4$ at 200−400 °C are shown in Figure 7. After 10 h test, the breakthrough curves reached 88%, 23%, 33%, 66%, and >90% at 200, 250, 300, 350, and 400 °C, respectively. At the optimal reaction temperature (250 °C), the concentration of elemental mercury abruptly decreased from about 1.06 mg Nm^{-3} to near zero in 60 min and reached 242 μg Nm^{-3} at the end of experiment (10 h).
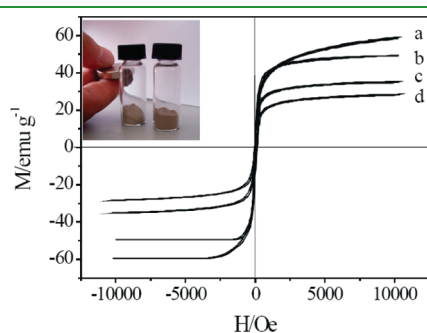

Figure 6. Magnetization characteristics of synthesized $(Fe_{3-x}Ti_x)_{1-\delta}O_4$: (a) $x = 0$; (b) $x = 0.3$; (c) $x = 0.7$; (d) $x = 1$. The insert shows the result of separating $(Fe_2Ti)_{0.8}O_4$ from the fly ash.

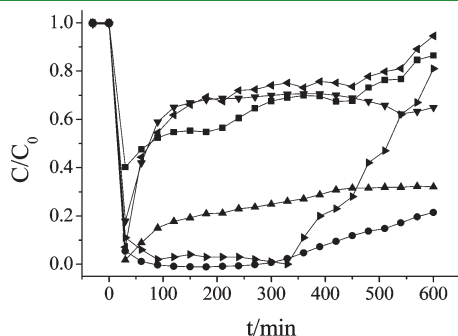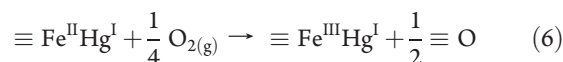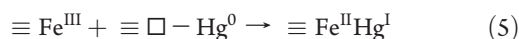**Figure 7.** Breakthrough curves of elemental mercury capture by $(Fe_2Ti)_{0.8}O_4$: ■, 200 °C; ●, 250 °C; ▲, 300 °C; ▼, 350 °C; (left-facing triangle), 400 °C; (right-facing triangle), 250 °C with SO_2.

The amount of elemental mercury captured per unit mass of sorbent (capacity) can be calculated from the breakthrough curve. The capacities of $(Fe_{3-x}Ti_x)_{1-\delta}O_4$ ($x = 0$, 0.3, 0.7, and 1) for elemental mercury capture under air are shown in Table 2. With the increase of Ti content in $(Fe_{3-x}Ti_x)_{1-\delta}O_4$, its capacity for elemental mercury capture obviously increased.

Elemental mercury capture by metal oxides in the absence of halogen may be attributed to Mars−Maessen mechanism.[15,18,52] Herein, the mechanism for elemental mercury capture by $(Fe_{3-x}Ti_x)_{1-\delta}O_4$ was studied using XPS. In comparison with fresh $(Fe_2Ti)_{0.8}O_4$ (shown in Figure 5a−c), no obvious changes happened in the XPS spectra over the spectral regions of Ti 2p, Fe 2p, and O 1s (shown in Figure 5d−f). Taking account of the binding energy of Hg4f 7/2 at 100.1 eV and the absence of Hg 4f 5/2 at about 105 eV corresponding to Hg^{2+} (shown in Figure 5g), the mercury adsorbed on $(Fe_2Ti)_{0.8}O_4$ may be mercurous oxide. Mercurous oxide has been previously observed on $(Fe_{2.2}Mn_{0.8})_{1-\delta}O_4$ and $(Fe_2Ti_{0.8}Mn_{0.2})_{1-\delta}O_4$ in our previous research.[53,54] The capture of elemental mercury by $(Fe_{3-x}Ti_x)_{1-\delta}O_4$ can be described as:

$$Hg^0_{(g)} + \equiv\square \longrightarrow \equiv\square - Hg^0_{(ad)} \tag{4}$$

$$\equiv Fe^{III} + \equiv\square - Hg^0 \longrightarrow \equiv Fe^{II}Hg^I \tag{5}$$

$$\equiv Fe^{II}Hg^I + \frac{1}{4}O_{2(g)} \longrightarrow \equiv Fe^{III}Hg^I + \frac{1}{2}\equiv O \tag{6}$$
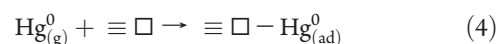
The overall reaction of gaseous elemental mercury capture is the sum of reactions 4−6:

$$Hg_{(g)} + \frac{1}{4}O_{2(g)} \xrightarrow{(Fe_{3-x}Ti_x)_{1-\delta}O_4} \frac{1}{2}Hg_2O_{(ad)} \tag{7}$$
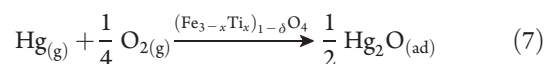
Cation vacancies on the surface ($\equiv\square$) are typical Lewis acid sites.[55] Gaseous elemental mercury is a Lewis base because it can be an electron-pair donor. The term Lewis base is more general and refers to the propensity to complex with a Lewis acid, so elemental mercury was first "physically" adsorbed on the cation vacancies (reaction 4). If the concentration of elemental mercury in the gas phase was sufficiently high for the surface to be saturated with physically adsorbed elemental mercury, the concentration of physically adsorbed elemental mercury on the surface ($[\equiv\square - Hg^0]$) can be described as

$$[\equiv\square - Hg^0] = k_1[\equiv\square] \tag{8}$$

where $[\equiv\square]$ and k_1 are the percent of cation vacancies on the surface and the constant, respectively. Reaction 4 is an exothermic reaction, so k_1 would rapidly decrease with the increase of reaction temperature.

Reaction 5 is the oxidation of physically adsorbed elemental mercury by Fe^{3+} cation on the surface ($\equiv Fe^{III}$) to form a surface Hg−Fe binary metal oxide ($\equiv Fe^{II}Hg^I$).[18] Because the oxidative capacity of Fe^{3+} cations was limited, the formed oxidized

Table 2. Capacity and Breakthrough Ratio of Synthesized $(Fe_{3-x}Ti_x)_{1-\delta}O_4$ for Elemental Mercury Capture (mg g^{-1})

$(Fe_{3-x}Ti_x)_{1-\delta}O_4$	200 °C	250 °C	300 °C	350 °C	400 °C
$x = 0$	0.26 ± 0.26 (>90%)	0.44 ± 0.44 (83%)	0.34 ± 0.34 (88%)	0.18 ± 0.18 (>90%)	0.04 ± 0.04 (>90%)
$x = 0.3$	0.48 ± 0.48 (>90%)	0.76 ± 0.38 (85%)	0.58 ± 0.29 (84%)	0.48 ± 0.25 (>90%)	0.40 ± 0.40 (>90%)
$x = 0.7$	1.14 ± 0.23 (>90%)	2.18 ± 0.33 (83%)	1.20 ± 0.24 (>90%)	0.70 ± 0.35 (>90%)	0.60 ± 0.30 (>90%)
$x = 1$	1.54 ± 0.31 (88%)	3.94 ± 0.39 (23%)	3.44 ± 0.34 (33%)	1.62 ± 0.32 (66%)	1.38 ± 0.28 (>90%)
$x = 1$ with SO_2	0.46 ± 0.23 (47%)	1.00 ± 0.20 (80%)	0.42 ± 0.21 (>90%)	0.36 ± 0.18 (>90%)	0.02 ± 0.02 (>90%)

mercury was mercurous oxide, which was demonstrated by XPS analysis (shown in Figure 5g). Reaction 6 was the reoxidization of formed Fe^{2+} cation. As is well-known, Hg_2O is not stable and it can self-decompose to HgO and Hg at a high temperature. Because the array of cation vacancies, Ti^{4+}, Fe^{3+}, and O^{2-} in/on $(Fe_{3-x}Ti_x)_{1-\delta}O_4$ was well-proportioned even at the atomic scale due to the incorporation of Ti cations into the spinel structure, the near two cation vacancies were spaced by many Ti^{4+}, Fe^{3+}, and O^{2-}. Because elemental mercury was adsorbed on the cation vacancy on $(Fe_{3-x}Ti_x)_{1-\delta}O_4$, the oxidized mercury formed on $(Fe_{3-x}Ti_x)_{1-\delta}O_4$ was isolated $Fe^{III}Hg^IO_2$. As a result, two mercurous cations can not collide to transform to one Hg atom and one Hg^{2+} cation. Therefore, the formed mercurous oxide on $(Fe_{3-x}Ti_x)_{1-\delta}O_4$ was stable.

The kinetic equation of reaction 5 can be described as

$$-\frac{d[\equiv Fe^{III}]}{dt} = -\frac{d[\equiv \square - Hg^0]}{dt} = k[\equiv Fe^{III}][\equiv \square - Hg^0]$$
$$= kk_1[\equiv Fe^{III}][\equiv \square] \qquad (9)$$

where $[\equiv Fe^{III}]$ and k are the concentrations of Fe^{3+} cations on the surface and the kinetic constant, respectively. Reaction 5 was promoted with the increase of reaction temperature, so k would increase with the increase of reaction temperature. The concentration of Fe^{3+} cations on $(Fe_{3-x}Ti_x)_{1-\delta}O_4$ was 8−9 times that of cation vacancies, so Fe^{3+} cations may be superfluous for elemental mercury oxidization. Therefore, eq 9 is approximately described as

$$-\frac{d[\equiv \square - Hg^0]}{dt} = -\frac{k_1 d[\equiv \square]}{dt} = k_2 k_1[\equiv \square] \qquad (10)$$

where k_2 is the kinetic constant.

According to eq 10, $[\equiv \square]$ can be approximately described as
$$[\equiv \square] = [\equiv \square]_0 \exp(-k_2 t) \qquad (11)$$

Then

$$-\frac{d[\equiv \square - Hg^0]}{dt} = k_2 k_1[\equiv \square]_0 \exp(-k_2 t) \qquad (12)$$

So

$$Q = BETk_2 k_1[\equiv \square]_0 \int_0^t \exp(-k_2 t) dt \qquad (13)$$

where Q is the amount of elemental mercury captured per unit mass of sorbent.

As shown in eq 13, the amount of elemental mercury captured was approximately proportional to the product of k_1, k_2, and the amount of cation vacancies on the surface (i.e., the product of BET surface area and $[\equiv \square]$). As shown in Table 1, the amount of cation vacancies increased with the increase of Ti content ($x \neq 0$). TPR analysis indicates that the reducibility of $(Fe_{3-x}Ti_x)_{1-\delta}O_4$ improved with the increase of Ti, so k_2 may increase with the increase of Ti in $(Fe_{3-x}Ti_x)_{1-\delta}O_4$. As a result, elemental mercury capture by $(Fe_{3-x}Ti_x)_{1-\delta}O_4$ was promoted with the increase of Ti (shown in Table 2).
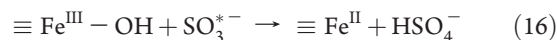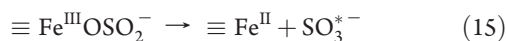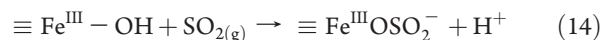
$(Fe_{3-x}Ti_x)_{1-\delta}O_4$ cannot be reduced at <200 °C (shown in Figure 4), so k_2 was very little at <200 °C. As a result, $(Fe_{3-x}Ti_x)_{1-\delta}O_4$ showed little ability for elemental mercury capture at <200 °C. Although k_2 increased with the increase of reaction temperature, k_1 decreased. As a result, elemental mercury capture by $(Fe_{3-x}Ti_x)_{1-\delta}O_4$ (reaction 7) would reach the optimal condition at a specific temperature, in most cases not the highest temperature.

The optimal temperatures for elemental mercury capture by $(Fe_{3-x}Ti_x)_{1-\delta}O_4$ all centered at about 250 °C.

Synthesized γ-Fe_2O_3 should show higher capacity for elemental mercury capture because the amount of cation vacancies on γ-Fe_2O_3 was much more than those on $(Fe_{2.7}Ti_{0.3})_{0.86}O_4$ and $(Fe_{2.3}Ti_{0.7})_{0.82}O_4$ (shown in Table 1). γ-Fe_2O_3 is metastable, and converts quickly to the thermodynamically stable form, hematite (α-Fe_2O_3), upon heating to 0−300 °C and/or compression.[8] During the capture of elemental mercury at 200−400 °C, structural strain arising caused spontaneous formation of α-Fe_2O_3 on γ-Fe_2O_3.[8] Once γ-Fe_2O_3 transformed to α-Fe_2O_3, cation vacancies on γ-Fe_2O_3 would disappear. So the real amount of cation vacancies on γ-Fe_2O_3 may be much less than it in Table 1 due to the formation of α-Fe_2O_3 during the test. In our previous research, it was demonstrated that the introduction of Ti had a stabilization effect on the spinel structure and the phase transition temperature of Ti-containing maghemite to Ti-containing hematite shifted to high temperature with the increase of Ti content in $(Fe_{3-x}Ti_x)_{1-\delta}O_4$.[5] So the formation of α-Fe_2O_3 would be suppressed due to the incorporation of Ti into γ-Fe_2O_3 structure. Furthermore, the constant k_2 of γ-Fe_2O_3 may be less than those of $(Fe_{2.7}Ti_{0.3})_{0.86}O_4$ and $(Fe_{2.3}Ti_{0.7})_{0.82}O_4$. As a result, $(Fe_{2.7}Ti_{0.3})_{0.86}O_4$ and $(Fe_{2.3}Ti_{0.7})_{0.82}O_4$ with lesser amounts of cation vacancies on their surfaces showed higher capacities for elemental mercury capture.

3.3. Effect of SO_2 on Elemental Mercury Capture. The capacity of $(Fe_2Ti)_{0.8}O_4$ for elemental mercury capture in the presence of 1000 ppmv of SO_2 is shown in Table 2. It shows that the presence of a high concentration of SO_2 resulted in obvious interference with elemental mercury capture by $(Fe_2Ti)_{0.8}O_4$.

Previous research postulated a mechanism for the heterogeneous uptake and oxidization of SO_2 on iron oxides,[56] and the reactions can be described as follows:

$$\equiv Fe^{III} - OH + SO_{2(g)} \rightarrow \equiv Fe^{III}OSO_2^- + H^+ \qquad (14)$$

$$\equiv Fe^{III}OSO_2^- \rightarrow \equiv Fe^{II} + SO_3^{*-} \qquad (15)$$

$$\equiv Fe^{III} - OH + SO_3^{*-} \rightarrow \equiv Fe^{II} + HSO_4^- \qquad (16)$$

Elemental mercury capture by $(Fe_2Ti)_{0.8}O_4$ in the presence of a high concentration of SO_2 was studied using XPS (shown in Figure 5h−l). As shown in Figure 5h, a new peak at 713.3 eV appeared in the spectral region of Fe 2p, which may be attributed to $Fe_2(SO_4)_3$. Once Fe^{3+} cations on $(Fe_2Ti)_{0.8}O_4$ transformed to $Fe_2(SO_4)_3$, the involved cation vacancies would be destroyed and cannot be regenerated. Therefore, the presence of a high concentration of SO_2 showed a significant interference with elemental mercury capture by $(Fe_2Ti)_{0.8}O_4$.

The formation of SO_4^{2-} can also be supported by the XPS spectra over S 2p and O 1s regions. The S 2p peaks (shown in Figure 5k) mainly centered at 168.4 and 170.1 eV, which may be assigned to SO_4^{2-} and HSO_4^-, respectively. Meanwhile, a subtle peak centered at 166.9 eV can be observed, which was ascribed to SO_3^{2-}. Furthermore, a new peak at 532.3 eV (shown in Figure 5j) appeared in the spectral region of O 1s, which may be assigned to SO_4^{2-}.

As shown in Figure 5l, the binding energy of the oxidized mercury formed in the presence of a high concentration of SO_2 centered at 101.1 eV. Taking account of the absence of Hg4f 5/2 at about 105 eV (corresponding to Hg^{2+}), the oxidized mercury formed was a mercurous compound. But the binding energy of

215

dx.doi.org/10.1021/am100835c |ACS Appl. Mater. Interfaces 2011, 3, 209–217

Hg_2O centers at 100.1 eV. Therefore, the oxidized mercury formed on $(Fe_2Ti)_{0.8}O_4$ in the presence of a high concentration of SO_2 may be Hg_2SO_4. It is noted that Hg_2SO_4 has been previously observed as a mercury product in a photochemical oxidation process for elemental mercury oxidation and capture.[24,57] Our previous research also demonstrated that mercurous sulfate formed during elemental mercury capture by $(Fe_{2.2}Mn_{0.8})_{1-\delta}O_4$ and $(Fe_2Ti_{0.8}Mn_{0.2})_{1-\delta}O_4$ in the presence of a high concentration of SO_2.[53,54]

XPS analysis showed that only 34% of Fe^{3+} cations on $(Fe_2Ti)_{0.8}O_4$ were sulfated after the test under a high concentration of SO_2. So $(Fe_2Ti)_{0.8}O_4$ still showed a moderate capacity (about 1.0 mg g^{-1} at 250 °C) for elemental mercury capture in the presence of 1000 ppmv of SO_2. When the inlet concentration of elemental mercury was about 0.45 mg Nm^{-3} (about 20 times that in the real flue gas), the removal efficiency of elemental mercury at 250 °C achieved >95% within 330 min (shown in Figure 7).

3.4. Future Study of the Application of $(Fe_2Ti)_{0.8}O_4$ for Elemental Mercury Capture. Previous research reported that Fe–Ti mixed oxide was a novel catalyst for the selective catalytic reduction of NO with NH_3 in the medium temperature range (200–400 °C) which was placed after the flue gas desulfurization (FGD).[58] In our future work, $(Fe_2Ti)_{0.8}O_4$ will be investigated to control the emission of NO_x. If $(Fe_2Ti)_{0.8}O_4$ is an excellent catalyst for the control of NO_x emission, it will be mainly used to control the emission of NO_x, and elemental mercury will be captured as a cobenefit. Therefore, the cost for the control of elemental mercury emission may be much lower.

Furthermore, the regeneration of the sorbent will be investigated. The formed oxidized mercury can be decomposed at about 500 °C. However, the phase transition of Fe–Ti spinel may occur and the magnetic property will disappear during the thermal treatment at 500 °C. In our future work, H_2 will be investigated to regenerate the sorbent at 300 °C. The adsorbed oxidized mercury may be reduced to gaseous elemental mercury by H_2. The concentration of elemental mercury in the exhaust of the regeneration may be much more than it in the flue gas, so it may be collected as liquid mercury at room temperature for safe disposal. $(Fe_2Ti)_{0.8}O_4$ may be reduced by H_2 to Fe_2TiO_4 at 300 °C. But $(Fe_2Ti)_{0.8}O_4$ can be recovered after the thermal treatment at 350 °C under air.

4. CONCLUSIONS

Cation-deficient Fe–Ti spinel has a large amount of cation vacancies on the surface, which may provide Lewis acid sites for the physical adsorption of elemental mercury. Then, the adsorbed elemental mercury is oxidized by Fe^{3+} cations on the surface to form oxidized mercury product, which adsorb on the surface. Furthermore, cation-deficient Fe–Ti spinel has a satisfactory saturated magnetization, which makes it possible to separate the sorbent from the fly ash to safely dispose the adsorbed mercury and regenerate the sorbent for recycling. As a result, cation-deficient Fe–Ti spinel may be a promising sorbent for the control of elemental mercury emission.

■ AUTHOR INFORMATION

Corresponding Author

*Phone: 86-21-54745591. E-mail: yangshijiangsq@163.com (S. J. Yang); nqyan@sjtu.edu.cn(N. Q. Yan).

■ ACKNOWLEDGMENT

■ REFERENCES

(1) Xu, Z. C.; Hou, Y. L.; Sun, S. H. *J. Am. Chem. Soc.* **2007**, *129*, 8698–8699.

(2) Lee, J. H.; Huh, Y. M.; Jun, Y.; Seo, J.; Jang, J.; Song, H. T.; Kim, S.; Cho, E. J.; Yoon, H. G.; Suh, J. S.; Cheon, J. *Nat. Med.* **2007**, *13*, 95–99.

(3) Son, S. J.; Reichel, J.; He, B.; Schuchman, M.; Lee, S. B. *J. Am. Chem. Soc.* **2005**, *127*, 7316–7317.

(4) Majetich, S. A.; Jin, Y. *Science* **1999**, *284*, 470–473.

(5) Yang, S.; He, H.; Wu, D.; Chen, D.; Liang, X.; Qin, Z.; Fan, M.; Zhu, J.; Yuan, P. *Appl. Catal., B* **2009**, *89*, 527–535.

(6) Yang, S. J.; He, H. P.; Wu, D. Q.; Chen, D.; Ma, Y. H.; Li, X. L.; Zhu, J. X.; Yuan, P. *Ind. Eng. Chem. Res.* **2009**, *48*, 9915–9921.

(7) Oliveira, L. C. A.; Fabris, J. D.; Rios, R.; Mussel, W. N.; Lago, R. M. *Appl. Catal., A* **2004**, *259*, 253–259.

(8) Cornell, R. M.; Schwertmann, U. *The Iron Oxides: Structure, Properties, Reactions, Occurrences and Uses*; Wiley-VCH: New York, 2003.

(9) Lindsley, D. H. *Oxide Minerals: Petrologic and Magnetic Significance*; Mineralogical Society of America: Chantilly, VA, 1991.

(10) Lee, W. J.; Bae, G. N. *Environ. Sci. Technol.* **2009**, *43*, 1522–1527.

(11) Romero, C. E.; Li, Y.; Bilirgen, H.; Sarunac, N.; Levy, E. K. *Fuel* **2006**, *85*, 204–212.

(12) Ji, L.; Sreekanth, P. M.; Smirniotis, P. G.; Thiel, S. W.; Pinto, N. G. *Energy Fuels* **2008**, *22*, 2299–2306.

(13) Lu, D. Y.; Granatstein, D. L.; Rose, D. J. *Ind. Eng. Chem. Res.* **2004**, *43*, 5400–5404.

(14) Wang, S. X.; Zhang, L.; Li, G. H.; Wu, Y.; Hao, J. M.; Pirrone, N.; Sprovieri, F.; Ancora, M. P. *Atmos. Chem. Phys.* **2010**, *10*, 1183–1192.

(15) Presto, A. A.; Granite, E. J. *Environ. Sci. Technol.* **2006**, *40*, 5601–5609.

(16) Li, Y.; Murphy, P. D.; Wu, C. Y.; Powers, K. W.; Bonzongo, J. C. J. *Environ. Sci. Technol.* **2008**, *42*, 5304–5309.

(17) Cao, Y.; Gao, Z.; Zhu, J.; Wang, Q.; Huang, Y.; Chiu, C.; Parker, B.; Chu, P.; Pan, W. P. *Environ. Sci. Technol.* **2008**, *42*, 256–261.

(18) Granite, E. J.; Pennline, H. W.; Hargis, R. A. *Ind. Eng. Chem. Res.* **2000**, *39*, 1020–1029.

(19) Lee, C. W.; Serre, S. D.; Zhao, Y.; Lee, S. J. *J. Air Waste Manage.* **2008**, *58*, 484–493.

(20) Strege, J. R.; Zygarlicke, C. J.; Folkedahl, B. C.; McCollor, D. P. *Fuel* **2008**, *87*, 1341–1347.

(21) Schofield, K. *Environ. Sci. Technol.* **2008**, *42*, 9014–9030.

(22) Qiao, S. H.; Chen, J.; Li, J. F.; Qu, Z.; Liu, P.; Yan, N. Q.; Jia, J. Q. *Ind. Eng. Chem. Res.* **2009**, *48*, 3317–3322.

(23) Lee, T. G.; Biswas, P.; Hedrick, E. *Ind. Eng. Chem. Res.* **2004**, *43*, 1411–1417.

(24) Granite, E. J.; Pennline, H. W. *Ind. Eng. Chem. Res.* **2002**, *41*, 5470–5476.

(25) Li, Y.; Murphy, P.; Wua, C. Y. *Fuel Process. Technol.* **2008**, *89*, 567–573.

(26) Lee, T. G.; Hyun, J. E. *Chemosphere* **2006**, *62*, 26–33.

(27) Mei, Z. J.; Shen, Z. M.; Wang, W. H.; Zhang, Y. J. *Environ. Sci. Technol.* **2008**, *42*, 590–595.

(28) Granite, E. J.; Myers, C. R.; King, W. P.; Stanko, D. C.; Pennline, H. W. *Ind. Eng. Chem. Res.* **2006**, *45*, 4844–4848.

(29) Granite, E. J.; Pennline, H. W.; Hoffman, J. S. *Ind. Eng. Chem. Res.* **1999**, *38*, 5034–5037.

(30) Granite, E. J.; King, W. P.; Stanko, D. C.; Pennline, H. W. *Main Group Chem.* **2008**, *7*, 227–237.

(31) Dong, J.; Xu, Z. H.; Kuznicki, S. M. *Adv. Funct. Mater.* **2009**, *19*, 1268–1275.

216

dx.doi.org/10.1021/am100835c |*ACS Appl. Mater. Interfaces* 2011, 3, 209–217

(32) Jones, A. P.; Hoffmann, J. W.; Smith, D. N.; Feeley, T. J.; Murphy, J. T. *Environ. Sci. Technol.* **2007**, *41*, 1365–1371.

(33) Milford, J. B.; Pienciak, A. *Environ. Sci. Technol.* **2009**, *43*, 2669–2673.

(34) Dong, J.; Xu, Z. H.; Kuznicki, S. M. *Environ. Sci. Technol.* **2009**, *43*, 3266–3271.

(35) Guigue-Millot, N.; Champion, Y.; Hytch, M. J.; Bernard, F.; Begin-Colin, S.; Perriat, P. *J. Phys. Chem. B* **2001**, *105*, 7125–7132.

(36) Perriat, P.; Fries, E.; Millot, N.; Domenichini, B. *Solid State Ion* **1999**, *117*, 175–184.

(37) Ayub, I.; Berry, F. J.; Crabb, E.; Helgason, O. *J. Mater. Sci.* **2004**, *39*, 6921–6927.

(38) Millot, N.; Aymes, D.; Bernard, F.; Niepce, J. C.; Traverse, A.; Bouree, F.; Cheng, B. L.; Perriat, P. *J. Phys. Chem. B* **2003**, *107*, 5740–5750.

(39) Li, J. F.; Yan, N. Q.; Qu, Z.; Qiao, S. H.; Yang, S. J.; Guo, Y. F.; Liu, P.; Jia, J. P. *Environ. Sci. Technol.* **2010**, *44*, 426–431.

(40) Yang, H. Q.; Xu, Z. H.; Fan, M. H.; Bland, A. E.; Judkins, R. R. *J. Hazard. Mater.* **2007**, *146*, 1–11.

(41) Presto, A. A.; Granite, E. J. *Environ. Sci. Technol.* **2007**, *41*, 6579–6584.

(42) Mei, Z. J.; Shen, Z. M.; Zhao, Q. J.; Wang, W. H.; Zhang, Y. J. *J. Hazard. Mater.* **2008**, *152*, 721–729.

(43) Presto, A. A.; Granite, E. J.; Karash, A. *Ind. Eng. Chem. Res.* **2007**, *46*, 8273–8276.

(44) Di Paola, A.; Bellardita, M.; Ceccato, R.; Palmisano, L.; Parrino, F. *J. Phys. Chem. C* **2009**, *113*, 15166–15174.

(45) Ji, Y. G.; Zhao, Z.; Duan, A. J.; Jiang, G. Y.; Liu, J. *J. Phys. Chem. C* **2009**, *113*, 7186–7199.

(46) Lin, H. Y.; Chen, Y. W.; Li, C. P. *Thermochim. Acta* **2003**, *400*, 61–67.

(47) Tiernan, M. J.; Barnes, P. A.; Parkes, G. M. B. *J. Phys. Chem. B* **2001**, *105*, 220–228.

(48) Park, E.; Ostrovski, O. *ISIJ Int.* **2004**, *44*, 999–1005.

(49) Silva, A. C.; Oliveira, D. Q. L.; Oliveira, L. C. A.; Anastacio, A. S.; Ramalho, T. C.; Lopes, J. H.; Carvalho, H. W. P.; Torres, C. E. R. *Appl. Catal., A* **2009**, *357*, 79–84.

(50) Zhang, Y.; Yang, M.; Dou, X. M.; He, H.; Wang, D. S. *Environ. Sci. Technol.* **2005**, *39*, 7246–7253.

(51) Herranz, T.; Rojas, S.; Ojeda, M.; Perez-Alonso, F. J.; Tefferos, P.; Pirota, K.; Fierro, J. L. G. *Chem. Mater.* **2006**, *18*, 2364–2375.

(52) Presto, A. A.; Granite, E. J. *Platinum Met. Rev.* **2008**, *52*, 144–154.

(53) Yang, S.; Guo, Y.; Yan, N.; Wu, D.; He, H.; Xie, J.; Qu, Z.; Jia, J. *Appl. Catal., B* **2011**, *101*, 698–708.

(54) Yang, S.; Yan, N.; Guo, Y.; Wu, D.; He, H.; Qu, Z.; Li, J.; Zhou, Q.; Jia, J. *Environ. Sci. Technol.* **2011** No. DOI: 10.1021/es103391w.

(55) Yang, S.; Guo, Y.; Yan, N.; Wu, D.; He, H.; Xie, J.; Qu, Z.; Yang, C.; Jia, J. *Chem. Commun.* **2010**, *46*, 8377–8379.

(56) Fu, H. B.; Wang, X.; Wu, H. B.; Yin, Y.; Chen, J. M. *J. Phys. Chem. C* **2007**, *111*, 6077–6085.

(57) McLarnon, C. R.; Granite, E. J.; Pennline, H. W. *Fuel Process. Technol.* **2005**, *87*, 85–89.

(58) Liu, F.; He, H.; Zhang, C. *Chem. Commun.* **2008**, *17*, 2043–2045.